RESEARCH ARTICLE

Macromolecular Bioscience
www.mbs-journal.de

Biosustainable Hybrid Nanoplatforms as Photoacoustic Agents

Giulio Pota, Paolo Armanetti, Brigida Silvestri, Bruno de Gennaro, Anna Zanfardino, Michela Di Napoli, Mario Varcamonti, Gianluca Landi, Alessandro Pezzella, Aniello Costantini, Giuseppina Luciani,* and Luca Menichetti*

The development of biosafe theranostic nanoplatforms has attracted great attention due to their multifunctional behavior, reduced potential toxicity, and improved long-term safety. When considering photoacoustic contrast agents and photothermal conversion tools, melanin and constructs like melanin are highly appealing due to their ability to absorb optical energy and convert it into heat. Following a sustainable approach, in this study, silver-melanin like-silica nanoplatforms are synthesized exploiting different bio-available and inexpensive phenolic acids as potential melanogenic precursors and exploring their role in tuning the final systems architecture. The UV–Vis combined with X-Ray Diffraction investigation proves metallic silver formation, while Transmission Electron Microscopy analysis reveals that different morphologies can be obtained by properly selecting the phenolic precursors. By looking at the characterization results, a tentative formation mechanism is proposed to explain how phenolic precursors' redox behavior may affect the nanoplatforms' structure. The antibacterial activity experiments showed that all synthesized systems have a strong inhibitory effect on *Escherichia coli*, even at low concentrations. Furthermore, very sensitive Photoacoustic Imaging capabilities and significant photothermal behavior under laser irradiation are exhibited. Finally, a marked influence of phenol nature on the final system architecture is revealed resulting in a significant effect on both biological and photoacoustic features of the obtained systems. These melanin-based hybrid systems exhibit excellent potential as triggerable nanoplatforms for various biomedical applications.

1. Introduction

Nanomaterials enable novel medical practices that allow for the early diagnosis and effective treatment of many diseases, with poor detrimental effects.[1–3] To achieve their biomedical aims, nanoplatforms often should be multifunctional: they should exhibit suitable contrast properties for selected imaging methods, target specific sites for therapeutic action, and ensure intrinsic safety.[4,5] To date, combination of different agents has achieved multiple functions; however, their uncontrolled disassembling in vivo may impair diagnostic accuracy and therapeutic efficacy.[6] The application of nanoparticles is limited due to their potential toxicity. Not only can nanoparticles (NPs) themselves raise long-term safety issues,[6,7] but also their synthesis often employs toxic moieties that may raise health and environmental concerns. The application of nanoparticles is limited due to their potential toxicity.[5,6] To meet this goal, significant breakthrough can be achieved by looking at nature as a source of cheap bioactive compounds and/or an inexhaustible font of inspiration to design biosafe multifunctional

G. Pota, B. de Gennaro, A. Costantini, G. Luciani
Department of Chemical
Materials and Production Engineering
University of Naples Federico II
Piazzale V.Tecchio, 80, Naples, NA 80125, Italy
E-mail: luciani@unina.it

P. Armanetti, L. Menichetti
Institute of Clinical Physiology
National Research Council
indirizzo Via G.Moruzzi 1, Pisa 56124, Italy

B. Silvestri
Department of Civil
Architectural and Environmental Engineering
University of Naples Federico II
Via Claudio, 21, Naples, NA 80125, Italy
E-mail: brigida.silvestri@unina.it

A. Zanfardino, M. D. Napoli, M. Varcamonti
Department of Biology
University of Naples Federico II
Via Vicinale Cupa Cintia, 21, Naples 80126, Italy

G. Landi
Istituto di Scienze e Tecnologie per l'Energia e la Mobilità Sostenibili
STEMS-CNR
Via Guglielmo Marconi, 4, Naples 80125, Italy

A. Pezzella
National Interuniversity Consortium of Materials Science and Technology (INSTM)
Via G. Giusti, 9, Florence 50121, Italy

The ORCID identification number(s) for the author(s) of this article can be found under https://doi.org/10.1002/mabi.202400013

DOI: 10.1002/mabi.202400013

materials with extraordinary performances for biomedical applications.[8–10] In this context, huge promise is held by melanin and melanin like moieties, including polyphenols, a class of ubiquitous pigments with native biocompatibility and unique multifunctional features encompassing photoprotection, free radicals scavenging, metal ions chelation, protein binding and even intrinsic antimicrobial activity.[4,9,11–15] They can be obtained by oxidative polymerization of a number of phenol derivatives, known as melanogenic precursors.[4,16] Particularly, outstanding ability of melanin like materials to absorb optical energy and convert it into heat, makes them highly attractive as dual agent, acting both as photo-acoustic and photothermal tool.[9,17] The development of Photoacoustic Imaging (PAI) methods and Photothermal Treatment (PTT) is particularly intriguing for medical and healing purposes. [4] To this purpose, promising outcomes are envisaged from optimizing melanin opto-electronic features. In this prospect, templated polymerization of melanogenic precursors, including 5,6-dihydroxyindole-2-carboxylic acid (DHICA), in the presence of a nanostructured ceramic phase proved to be a successful approach to tune the supramolecular structure of melanin like moieties, leading to hybrid melanin-based materials with improved biological and chemical features.[18–20] At the same time, metal-polyphenol complexes lead to self-assembled supramolecular architectures, which not only are able to manage metal toxicity but also exhibit a marked optical absorption enhancement mediated by ligand to metal charge transfer phenomenon, thus resulting in enhanced photothermal properties.[8] Furthermore, the redox activity of melanin like moieties can be effectively exploited for metal cations reduction, leading to metal nanoclusters which concur to improve photoacoustic and photothermal performance.[21–23] Synergistic integration of these approaches has recently enabled the design of hybrid ternary silver (core)-melanin/silica (shell) NP exhibiting higher photoacoustic contrast properties than neat DHICA-eumelanin and silver nanoclusters.[19] Promising results led us to conduct further research to improve silver-melanin like-silica NPs' design, creating effective platforms for biomedical imaging techniques like MRI and PA. To explore cheaper and more sustainable theranostic tools, this study investigated different phenol moieties to build up the organic component in the ternary system. Notably, in addition to DHICA, which was obtained by laboratory synthesis, bio-available caffeic acid and gallic acid were explored as potential melanogenic precursors. Both compounds are gaining popularity in different fields of application, including human health. Caffeic acid is a potent antioxidant and anti-inflammatory compound, gallic acid is known for its remarkable pharmacological activities, such as antitumor, anti-inflammation, immune regulation, anti-oxidation, antidiabetes, liver protection, and cardioprotective effects. However, some restricting properties, such as limited solubility, absorption, bioavailability, instability, lack of specificity, and high systemic clearance, still hinder their use. The proposed hybrid systems can overcome these limitations by protecting these compounds from degradation and masking their limiting physicochemical properties.

Additionally, more sustainable and environmentally friendly method has been adopted as alternative for the typical hazardous synthesis pathway of melanogenic precursor (i.e., DHICA). The use of waste-derived compounds ensures not only less harmful but also more economical process.

Prepared nanoplatforms were submitted to detailed physicochemical characterization to assess morphology, structure and optical features. Photoacoustic and photothermal properties were determined and compared evidencing good performance for all investigated systems. In addition, antioxidant and antibacterial features were evaluated to assess multifunctional behavior of prepared nanostructures. Indeed, in-depth morphological investigation through SEM analysis evidenced a marked influence of phenol nature on the final system architecture, which resulted in a significant effect on biological and photoacoustic features.

2. Experimental Section

2.1. Materials

EDC (protein seq grade), NHS (98%), APTS, TEOS (99.999%), ammonium hydroxide (NH_3, Lsg ACS reagent 28−30%), ethanol (absolute, ≥99.8%), caffeic acid (≥98.0%), and gallic acid (97.5–102.5% titration) were purchased from Sigma-Aldrich and used as received. DHICA monomer was prepared as described elsewhere.[24]

2.2. Synthesis of Hybrid Silica-Based Nanoplatforms

Inspired by the previous works,[16,22] the hybrid nanoplatforms were produced using an in-situ sol-gel route. APTS-organic monomer (i.e., DHICA, CAF or GAL) hybrid precursors were first synthesized through EDC/NHS chemistry.[25] Carboxyl (–COOH) groups of organic monomers were coupled to amino groups of APTS molecules [19] followed by the addition of DHICA, CAF or GAL (2.2 mM) and TEOS (87 mM) in ethanol. Afterwards, $AgNO_3$ (corresponding to DHICA:Ag^+ ratio = 1:1 mol:mol) in water solution were added, and the pH value was adjusted to 9.5 by adding a mixture of ammonia in ethanol. After 18 h at room temperature, hybrid NPs were recovered by centrifugation and repeatedly washed (three times with distilled water). The synthesized samples will be indicated in the following as DHICA-Ag_SiO_2, CAF-Ag_SiO_2 and GAL-Ag_SiO_2 NPs.

2.3. Characterization

Transmission Electron Microscopy (TEM) was used to investigate NPs morphology. About 10 µL of aqueous solution containing NPs was spread on a copper grid (200 mesh with carbon membrane). TEM images were obtained using a TECNAI 20 G2: FEI Company with a camera Eagle 2HS. The images were acquired at 200 kV; camera exposure time: 1 s; size

A. Pezzella
Institute for Polymers
Composites and Biomaterials (IPCB)
CNR
Via Campi Flegrei, 34, Pozzuoli, NA 80078, Italy
A. Pezzella
Department of Physics Ettore Pancini
University of Naples Federico II
Via Vicinale Cupa Cintia, 21, Naples 80126, Italy

≈2048 Å. ζ-potential investigations were performed through Zetasizer instrument (Nanoseries, Malvern) using the particle electrophoresis technique. All the samples were diluted up to a droplet concentration of approximately 0.025% w/v by using Milli-Q water. ζ-potential analyses were carried out by setting 50 runs for each measurement. The analysis of energy dispersive X-ray spectroscopy (EDX) involved depositing a suspension of nanoparticles onto an aluminum stub, and subsequently applying a Pt/Pd layer (5 nm) through sputter-coating using a Cressington sputter coater 208HR. Following this preparation, the specimens underwent examination using a Field Emission Ultrapluss ZEISS Microscope. The determination of the total phenolic content (TPC) in both systems involved the use of the Folin–Ciocalteu reagent (FCR), a combination of sodium phosphomolybdate ($Na_3PMo_{12}O_{40}$)and sodium phosphotungstate ($Na_3PW_{12}O_{40}$), typically yellow.[26] Reduced by substances with phenolic groups, FCR undergoes a color change to blue, and the maximum absorbance at 765 nm is proportional to the overall phenolic compound content. The test, conducted at pH 10, entails combining phenolic compounds (0.75 mg mL^{-1}) and FCR with a Na_2CO_3 75 mg mL^{-1} solution (final volume ratio of 1:3:14). Notably, under alkaline conditions, phenols dissociate into phenolate anions, facilitating the reduction of FCR. The outcomes are quantified as micrograms of gallic acid equivalent per gram of the sample, with gallic acid serving as the reference standard. The reaction mixture is incubated at 40 °C for 30 min, followed by the measurement of absorbance at 765 nm, end the gallic acid equivalents were calculated after drawing a calibration curve. All experiments were conducted in triplicate. Fourier transform infrared transmittance (FT-IR) spectra were obtained by using a Nexus FT-IR spectrometer connected to DTGS KBr detector. Pellets of 200 mg were obtained by dispersing 0.5 mg of the NP in KBr, and all spectra were recorded in the 4000–400 cm^{-1} range, with a 2 cm^{-1} value of resolution, and KBr was used as the blank. Thermogravimetric analysis (TGA) and Differential Scanning Calorimetry (DSC) were used to investigate the thermal behavior of samples by using a TA instrument simultaneous thermoanalyser SDT Q600 (TA Instrument, New Castle, DE, USA). 10 mg of each sample were placed in a platinum pan and tested under nitrogen atmosphere, in a temperature range between 25 and 700 °C with a heating rate of 10 °C min^{-1}. BET specific surface areas (SSA) of NP were measured by N_2 adsorption at 77 K with a Quantachrome Autosorb-1C instrument. All samples were degassed at 150 °C for 3 h. Content of silver in all synthesized samples was analyzed by using Plasma Emission Spectrophotometry, ICP-OES Perkin-Elmer Optima 2100DV. An appropriate amount of each system was first subjected to acid digestion in 10 mL of a solution containing HNO_3, HCL, and HF in suitable ratios, and then the supernatant was analyzed at the most sensitive Ag wavelengths (243.778, 328.068, 338.289 nm). The test was made in triplicate and the results are an average of the whole runs.

2.4. Biological Assay

The antimicrobial activity of NSs samples was evaluated against Escherichia coli DH5a.[27] NPs suspensions were sonicated on ice with a tip-sonicator at 50% amplitude for 10 min (alternating 30 s on/off) before preparing the mixture with bacteria. In dose–response curves, the samples were prepared by adding bacterial cells and NSs at different concentrations (from 0 to 200 μg mL^{-1}), in a phosphate buffer at pH 7.4. Negative control was represented by cells with any treatment. Samples were incubated at 37 °C for 4 h, were placed on solid medium LB agar and incubated overnight at 37 °C. The following day the surviving cells were estimated by colony counting on each plate and compared with the controls.[28] Standard deviations were less than 5% for each experiment (which was performed at least in triplicate).

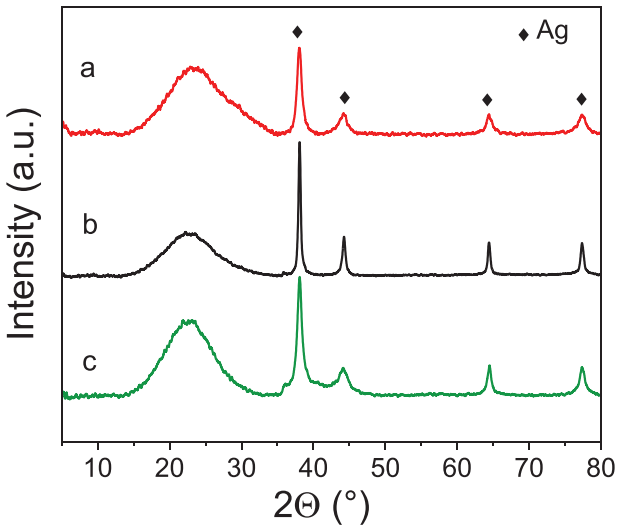

Figure 1. XRD spectra of DHICA-Ag_SiO_2 a), CAF-Ag_SiO_2 b) and GAL-Ag_SiO_2 c) NPs.

Table 1. Ag concentration by ICP-OES analysis.

Sample name	Ag Amount (μg/mg)
DHICA-Ag_SiO_2	27.5 ± 1.4
CAF-Ag_SiO_2	29.7 ± 1.5
GAL-Ag_SiO_2	31.8 ± 1.6

2.5. Photoacoustic and Ultrasound Measurements

Photoacoustic and ultrasound measurements were carried out with a multimodal imaging platform Vevo lAZR-X from VisualSonics Inc. (VevoLAZR, FUIJIFILM VisualSonics Inc., Toronto, ON, Canada), producing PA images co-registered with B-mode images. PA signals were excited by laser pulses of 6–8 ns pulse width generated at a rate of 20 Hz. The PA platform works in in two near-infrared windows from 680 to 970 nm, from 1200 up to 2000 nm.[19]

2.6. Ex-Vivo PAUS Assessment

Ex vivo investigations were performed on chicken breast samples, to simulate biological environment conditions. The chicken breast samples were injected with a bolus of around 30 μL for each kind of nanoplatforms. The samples were

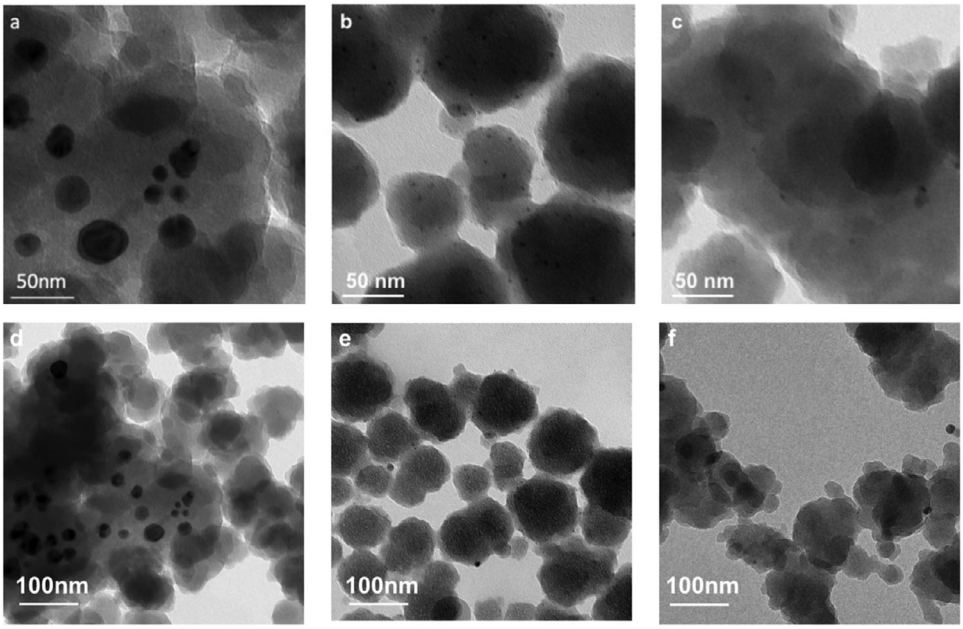

Figure 2. TEM micrographs of DHICA-Ag_SiO_2 a,d), CAF-Ag_SiO_2 b,e) and GAL-Ag_SiO_2 c,f) NPs at different magnification.

then imaged by photo-acoustics, getting PA spectral analysis (PSA) and PHS, evaluating the PA Signal distribution inside the whole injected volumes throughout multiwavelength PA stimulation.

2.7. Spectrophotometer Analysis

The optical properties of nanopletforms were also studied, acquiring the absorbance spectrum by a spectrophotometer analysis by Tecan infinite 200 PRO.

2.8. Hyperthermic Evaluation

The NP were loaded in polystyrene cuvettes, then placed in a cuvette holder inside a custom-made laser line setup. The cuvettes were illuminated for around 15 minutes by 300 mW laser light at 808 nm, then kept them cool down for ten minutes at room temperature. The thermal behaviors during the heating (laser on) and cooling (laser off) have been recorded by a thermocamera (heimann sensors), placed in front of the large side of the cuvette. The laser illumination was released on the short side of the cuvettes. The thermal dataset was being processed by a custom-made algorithm in Matlab.

3. Results and Discussion

3.1. Physic-Chemical Characterization

Figure 1 showed the XRD patterns of synthesized samples. A broad band ranging from 15 to 30° in 2θ angle, which was consistent with the silica's amorphous structure can be observed in all spectra.[29] In addition, four diffraction peaks are also located at 2θ = 38, 44, 64, and 77° and attributed to (111), (200), (220), and (311) planes of Ag crystals, respectively, indicating the presence of silver crystals with face-centered cubic structure in the hybrid nanostructures.[30] These results proved the involvement of phenolic components in reducing Ag^+ ions to metallic Ag, as reported in literature.[31,32]

The Ag contents obtained by ICP analysis are reported in **Table 1** and expressed as μg of Ag per mg of NP.

The obtained results showed no significative differences in the amount of Ag in each sample. In addition, Scanning Electron Microscopy-Energy Dispersive X-ray analysis (Figure S1, Supporting Information) was performed to confirm the elemental compositions of all synthesized systems. As reported in Table S1 (Supporting Information), all samples had an almost similar composition. However, Ag atomic % for DHICA-Ag_SiO_2 is more than twice the values for CAF- and GAL-Ag_SiO_2, suggesting higher chelating and reducing power for the eumelanin precursor.

The morphology of all synthesized samples was examined by Transmission Electron Microscopy (TEM). **Figure 2** shows the TEM images of DHICA-Ag_SiO_2 (a), CAF-Ag_SiO_2 (b), and GAL-Ag_SiO_2 (c) NPs. Different contrast areas could be seen for all samples: small black areas, attributed to the metallic Ag domains, and pseudo-spherical less dense larger particles with rough surfaces. More in detail, in the TEM image of DHICA-Ag_SiO_2 sample (Figure 2a), the metallic Ag domains (ranging from 5 to 40 nm in diameter) are apparently located in the core of NP and coated with a less dense silica layer. This structure is in accordance with that evidenced by samples with comparable compositions and obtained using the same synthesis approach.[19] On the other hand, a different structure was observed in the case of CAF-Ag_SiO_2 sample (Figure 2b) where small Ag domains, about 5 nm in average size, appeared uniformly dispersed on the surface of silica

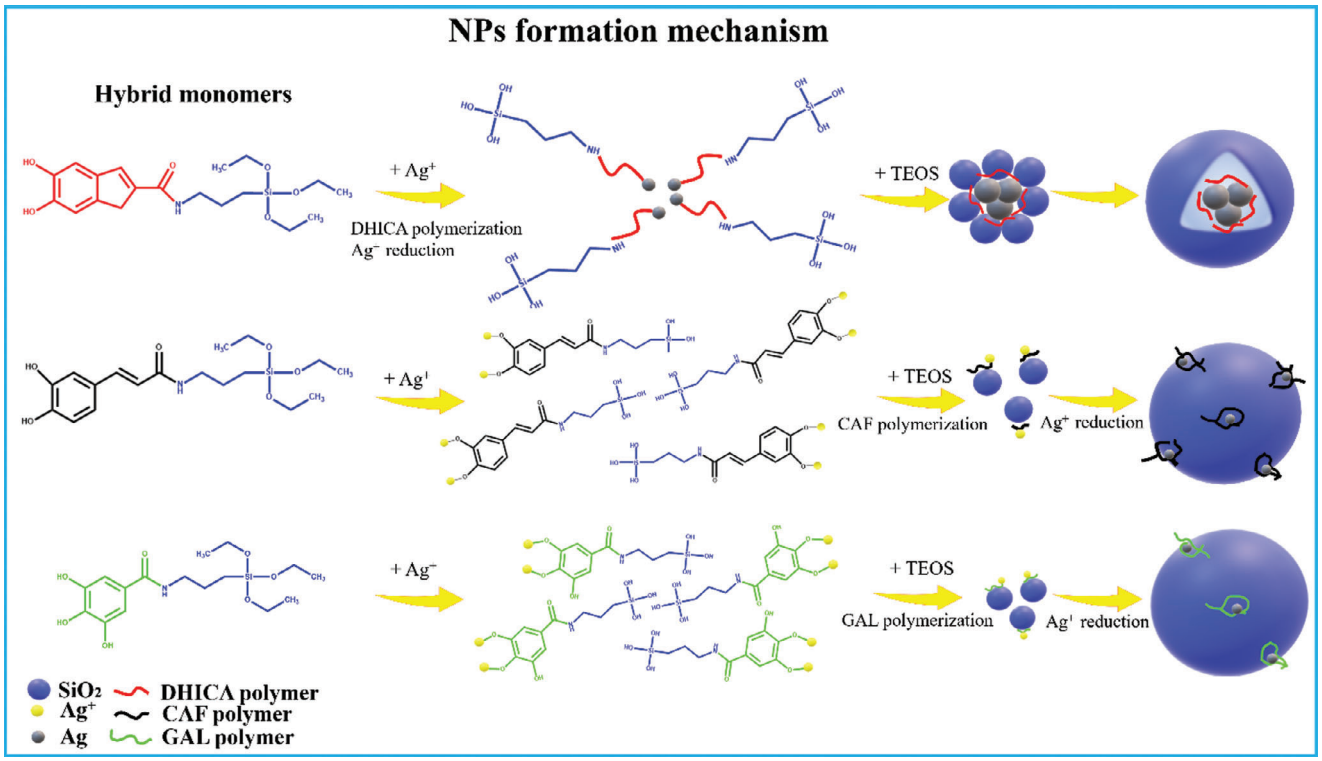

Scheme 1. Schematic representation of hybrid NP formation.

NP, rather than in the core. A similar structure could be appreciated in the micrography of GAL-Ag_SiO_2 sample (Figure 2c); yet the number of Ag seeds significantly decreased and only a few of them can be appreciated.

These results suggest that the pristine APTS-phenolic hybrid precursors have different efficacy in the reduction of silver ions under the same synthesis conditions. Following the hybrid monomer synthesis, all other reagents are gradually added to the reaction mixture; therefore, silica and metal components form concurrently. Thus, the formation kinetics of both silica and metal components are expected to strongly influence the final architecture of the NPs. A proposed formation mechanism of all hybrid systems is illustrated in **Scheme 1**.

Under alkaline conditions, phenols deprotonate, producing phenolate anions. [33] These species undergo electrophilic aromatic substitution by transferring electrons to Ag^+ ions to form metallic Ag^0. [34,35] The reduction potential of phenolic acids is directly related to number and position of their functional hydroxy groups.[36] In addition, the electron-donating activity of melanin-polymers was found to be very different from than that of monomeric precursors. When DHICA monomer is used, the color solution quickly changes to black, immediately after the addition of $AgNO_3$, due to the reduction of Ag^+ into metallic Ag° concurrently with DHICA oxidation, which leads to its polymerization, resulting in DHICA-melanin formation. [19] Due to the rapid local increase in Ag° concentration, the nucleation and aggregation of silver nanodomains easily lead to the assembly and growth of the metallic Ag species into large-sized Ag nanodomains. These are supposed to act as nucleation sites for the subsequent formation of silica surface layer, in agreement with TEM micrography of Figure 2a, where a core-shell structure is clearly observed. When caffeic or gallic acids are used, after the addition of silver salt, there is no rapid color change observed and the solution gradually becomes opalescent and gray. **Figure 3** reported the UV-vis spectra of all organic monomers in similar reaction conditions without Ag (DHICA/CAF/GAL_t0), immediately (DHICA/CAF/GAL-Ag_t0) and 18 h (DHICA/CAF/GAL-Ag_18 h) after the addition of $AgNO_3$ (all spectra were recorded in the absence of only silica precursor).

As can be seen, both CAF-Ag_t0 and GAL-Ag_t0 spectra (Figure 3b,c) do not show any appreciable absorption peak in the wavelength region 300 nm to 600 nm, however a broad absorption band, centered at ≈430 nm, was observed for DHICA-Ag_t0 sample (Figure 3a). This absorption band is related to the localized surface plasmon resonance (SPR) [37–39] indicative for silver particles, thus confirming the rapid formation of Ag domains in DHICA sample. The UV–Vis spectrum of DHICA sample (Figure 3a, black line) exhibits no significant changes after 18 h of reaction, whereas both CAF and GAL samples show the presence of a shoulder located at ≈400 and 450 nm, respectively (Figure 3b,c black lines). Typically, SPR intensity, position and shape depend of several factors such as size, shape and agglomeration of metallic NP, thus, these results prove the formation of Ag domains, in both CAF and GAL samples over a longer time period than DHICA [40]. From this experimental evidence it may be inferred that the reduction kinetics of silver by both gallic and caffeic acid is slower than that appreciated for DHICA. Hence, it is reasonable to assume that when DHICA monomer is used, polymerization of organic components and silver reduction occur before silica particles formation, on the other hand for

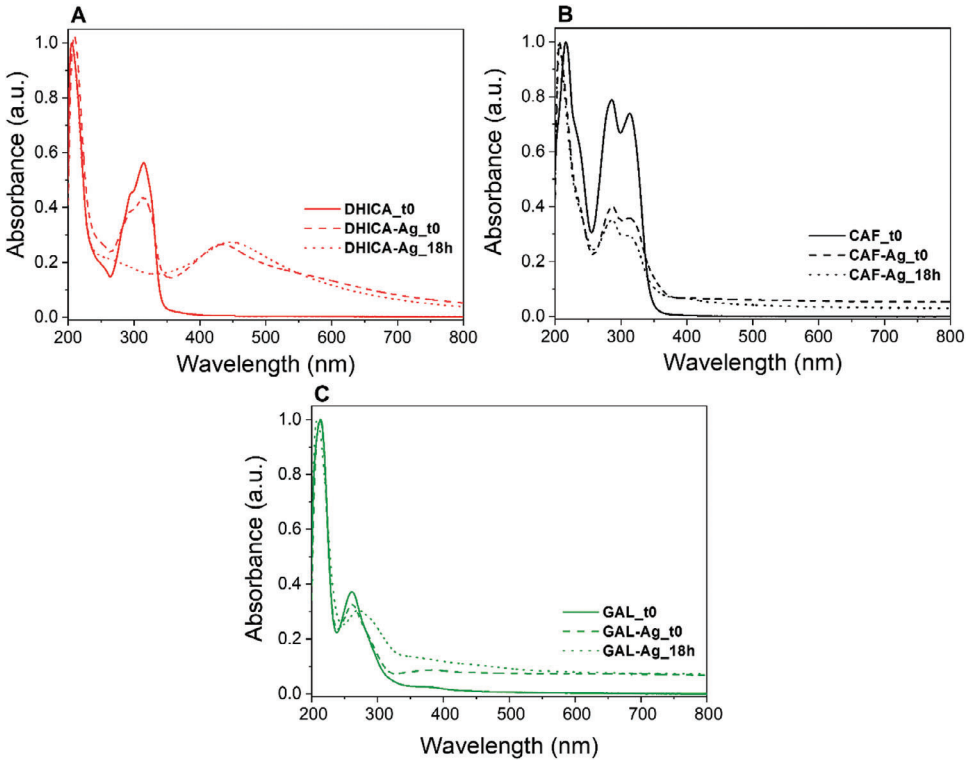

Figure 3. UV–Vis spectra of DHICA a), CAF b), and GAL c) monomers in similar reaction conditions without Ag (continuous line), immediately (dashed line) and 18 h (dotted line) after the addition of $AgNO_3$.

Table 2. SSA, ζ−potential and amount of gallic acid equivalent for hybrid NPs.

Sample name	SSA (m^2/g)	ζ-Pot (mV)	Gallic acid equivalent/ sample (μg/g)
DHICA-Ag_SiO_2	79 ± 5	−12.3 ± 0.65	230 ± 20
CAF-Ag_SiO_2	55 ± 4	−45.4 ± 1.47	325 ± 15
GAL-Ag_SiO_2	66 ± 5	−46.4 ± 1.21	283 ± 15

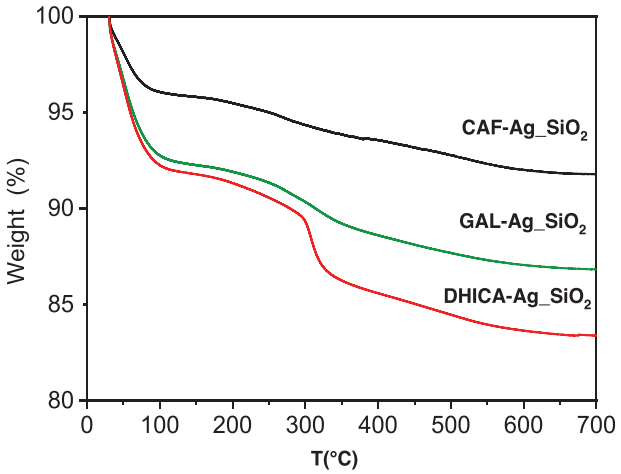

Figure 4. TGA curves of DHICA-Ag_SiO_2, CAF-Ag_SiO_2 and GAL-Ag_SiO_2 NP.

CAF and GAL monomers, silica formation probably occurs before the metal reduction, leading to the production of small Ag domains on the surface of faster preformed silica particles, as reported in the Scheme 1. The SSA, ζ-potential of all NPs and results of Folin-Ciocâlteu assay are reported in **Table 2**. The surface area values fall in the range of 50–80 m^2 g^{-1}. DHICA-Ag_SiO_2 NP showed the highest SSA: the preformed melanin-Ag nanodomains influence the subsequent formation of the silica shell leading to different textural properties. The results of the zeta potential analysis of all NP showed negative surface charge values (Table 2). The lowest absolute value of ζ-potential (−12.3 mV) was observed in DHICA-Ag_SiO_2 NP, while both CAF-Ag_SiO_2 and GAL-Ag_SiO_2 NP showed the highest absolute value of zeta potential (≈−45 mV). These different values could be due to the presence of different exposed negatively charged groups onto the surface of NP. As described in the proposed formation mechanism of nanoplatforms, the reduction of silver and subsequent development of metallic clusters may be driven by the organic component, which ultimately determines the position of the Ag domains into the NP. The Folin–Ciocâlteu assay was performed to determine the content of exposed phenolic groups in all synthesized systems and the results, reported in Table 2, revealed the highest amount of these groups in both CAF and GAL samples. The highest number of hydrolysable groups on the surface of CAF-Ag_SiO_2 and GAL-Ag_SiO_2 NPs might be responsible for the highest absolute value of ζ-potential. In addition, the metallic phase is prevalently located on the surface of the CAF and GAL

Table 3. Organic content estimated from TG analysis.

Sample	Organic %wt.
DHICA-Ag_SiO_2	10.0 ± 0.7
CAF-Ag_SiO_2	4.5 ± 1.1
GAL-Ag_SiO_2	6.4 ± 0.6

samples, maybe due to the higher concentration of the organic component on these NP than on the DHICA sample. This supports our hypothesis of differing surface organization of organic and inorganic components, as a consequence of their different formation kinetics.

TGA analysis was performed to assess the organic content in the hybrid systems and the obtained weight loss profiles were reported in **Figure 4**.

All TGA curves showed a low-temperature weight loss in the range of 25–100 °C, of ≈4% wt. in CAF-Ag_SiO_2 sample and 8.0% wt. in both DHICA and Gal-Ag_SiO_2 samples, related to the removal of physically adsorbed water. By increasing the temperature, additional weight loss was visible in the range 200–650 °C, attributed to both decomposition of organic components [41] and dehydroxylation of Si–OH residual groups, forming Si–O–Si groups[42]. As reported in **Table 3** different amount of the organic phase was estimated in the produced hybrid NPs.

Compared with both CAF-Ag_SiO_2 and GAL-Ag_SiO_2 samples, the weight loss of DHICA-Ag_SiO_2 NPs, related to the organic component, was markedly larger (10.0% wt.), Indeed, as reported in Table 3, the amount of organic phase in both other samples can be determined to be about 5% wt. This result should be accounted by the fast formation of DHICA melanin-silver clusters. Acting as nucleation centers, the silica shell might likely grow and trap these components, thus avoiding their release. On the other hand, in both CAF- and GAL-Ag_SiO_2 samples, the silica formation kinetics is probably comparable with organic phase polymerization. In addition, polymerization is triggered by the alkaline environment rather than by metal reduction. Therefore, isolated melanin-like domains are formed in the reaction mixture and probably lost during the washing steps. Lastly, the higher inflection point, observed in the degradation temperature range of organic component in DHICA-Ag_SiO_2 sample, proved a protective action of the outer silica layer.

3.2. Antimicrobial Activity

Silver-containing hybrid nanostructures were tested in antimicrobial assays. To evaluate this aspect, vital bacterial counting experiments were performed, using *Escherichia coli* as a model strain. Samples containing three types of NPs (DHICA-Ag_SiO_2, CAF-Ag_SiO_2, Gal-Ag_SiO_2) were used at different concentrations, starting from zero – the experiment control – up to a

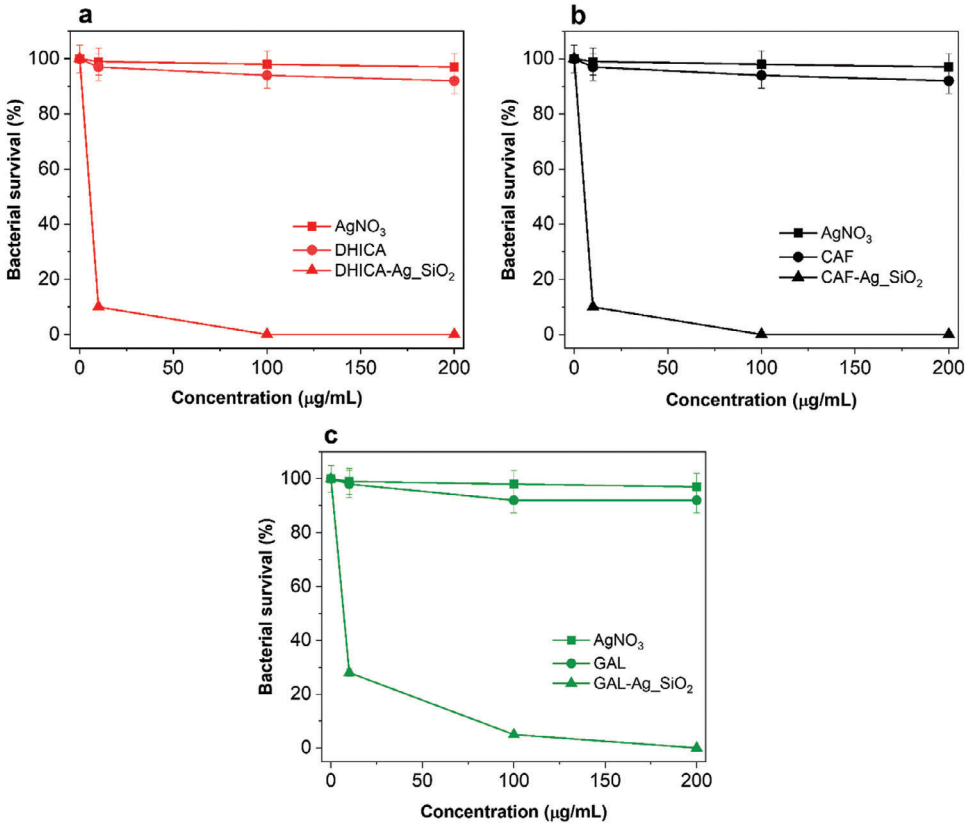

Figure 5. Antimicrobial activity of DHICA-Ag_SiO_2 a), CAF-Ag_SiO_2 b), Gal-Ag_SiO_2 c) and respective controls at different concentrations (0–200 μg mL^{-1}) evaluated by colony count assay, after 4 h of incubation, against *Escherichia coli* DH5a strain. The % of bacterial survival is represented on the y-axis. The assays were performed for three independent experiments.

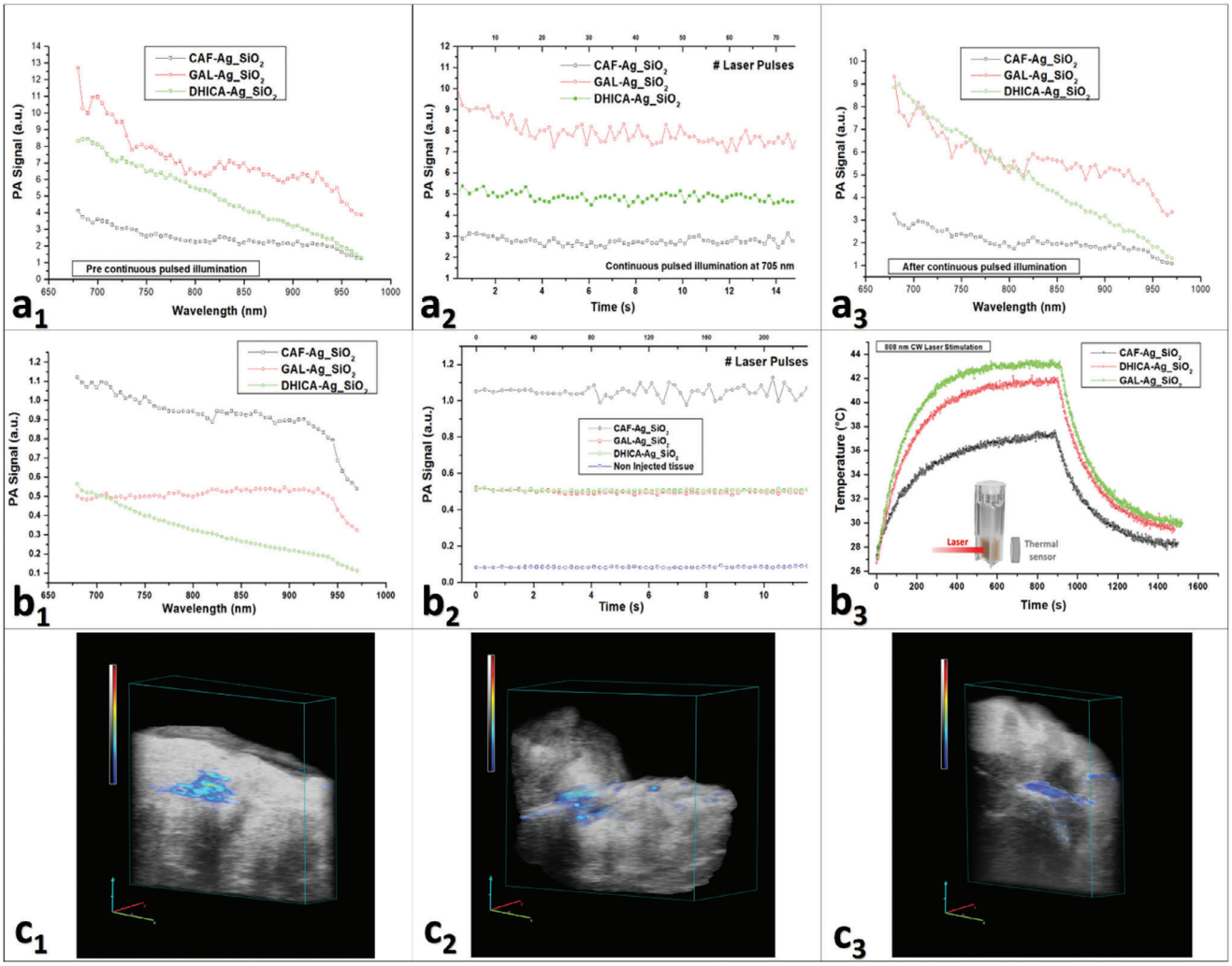

Figure 6. The PA tests carried out in PE tubes for material characterization are shown in the first row, respectively, PA spectral trend a_1) and pre and post continuous pulsed laser illumination a_2,a_3); in the second row, panels b_1 and b_2 report the PA response obtained inside three different ex-vivo samples of chicken breast injected with NPs bolus to simulate a real environment, then the plot b_3 of the thermic raising properties of NPs under CW laser illumination in cuvette; the last row shows the 3D PAUS volume reconstruction of three sample of chicken breast injected with the NPs, gray scalebar for US signal, rainbow scalebar for PA signal.

maximum of 200 μg/ml. **Figure 5** shows the various concentrations of NP (*x*-axis) related to the cell survival (*y*-axis). In addition to the NPs, the relative controls are shown: the silver salt ($AgNO_3$) and the respective precursor, used for the synthesis of the NP themselves. DHICA (panel a), CAF (panel b), and GAL (panel c), all of them used as a precursor, are shown in Figure 5. As shown in this figure, all the different nanoplatforms are active against the bacterium indicator even at low concentrations. The NP containing DHICA and CAF are more active than the Gallic acid ones, in accordance with the NP different structure. As previously reported in the micrography of the sample Gal-Ag_SiO_2 (Figure 2c), the number of small Ag nanoparticles has significantly decreased. In all three panels, the respective controls do not seem to have any significant antimicrobial activities: both the silver salt and the NP precursors (DHICA, CAF and GAL) were used at the same concentrations as the whole nanoplatforms.

3.3. Photoacoustic In-Vitro Tests

The typical PA spectra and the Photostability (PHS) of DHICA-Ag_SiO_2, CAF-Ag_SiO_2, Gal-Ag_SiO_2 NPs are presented in **Figure 6** (a_1,a_3,b_1).

As expected, the spectra reflect the optical trends got by the spectrophotometer analysis (**Figure 7**).

Indeed, the PA effect is strictly related with the optical properties of the materials; the magnitude of the stimulated acoustic wave pressure is proportional to the optical absorption coefficient specific of the sample under study. The first row of the Figure 6 shows the PA acquisition got by the different NPs (DHICA-Ag_SiO_2, CAF-Ag_SiO_2, Gal-Ag_SiO_2) loaded in the PE tubes in the water box phantom. Specifically, two sets of spectral acquisitions were reported (Figure $6a_1$,a_3) acquired before and after the PHS test (Figure $6a_2$), consisted in a continuous laser illumination at fixed wavelength (705 nm), for over 200 laser

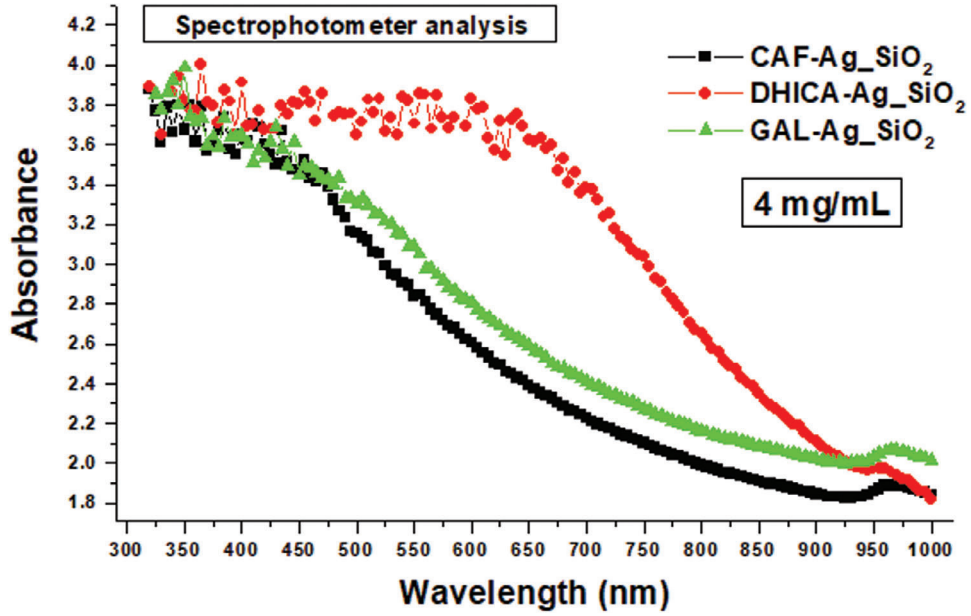

Figure 7. Spectrophotometer: Plot of the absorbance optical properties of DHICA-Ag_SiO_2, CAF-Ag_SiO_2 and GAL-Ag_SiO_2 NPs.

Table 4. PA NPs characterization in PE tubes: PA mean values and standard deviation obtained during PHS investigations by illuminating at 705 nm, contrast-to-noise ratio (CNR), signal-to-noise-ratio (SNR), and percentage variation coefficient.

NPs concentration 4 mg/mL	PA Signal (a.u.)	St.Dev.	CNR	SNR	%CV
CAF-Ag_SiO_2	2.76896	0.17535	15	16	6.3
GAL-Ag_SiO_2	7.75542	0.62876	12	12	8.1
DHICA-Ag_SiO_2	4.86367	0.18822	26	26	3.9

Table 5. PA NPs characterization in biological environment: PA mean values and standard deviation obtained during PHS investigations by illuminating at 705 nm, contrast-to-noise ratio (CNR), signal-to-noise-ratio (SNR), and percentage variation coefficient.

NPs 4 mg/mL	PA Signal (a.u.)	St.Dev.	CNR	SNR	%CV
CAF-Ag_SiO_2	1.05063	0.03553	27	29	3.4
GAL-Ag_SiO_2	0.49592	0.00847	49	58	1.7
DHICA-Ag_SiO_2	0.50624	0.00443	95	114	0.9

shots. The PHS tests represents a crucial point of assessment, indeed the spectral fingerprint of the nanoparticles could instantaneously get alterations due to the strong interactions of pulsed light and their plasmonic resonance. As showed in the spectral trends (Figure 6,a1,a3), the NPs didn't suffer of spectral modifications, and in terms of the PA signal intensities there weren't significant variations (Table 3). The contrast to noise and signal to noise ratio calculations (CNR, SNR) were reported in the **Table** 4. In comparison with CAF and Gal-Ag_SiO_2 nanoparticles, the DHICA-Ag_SiO_2 nanoparticles showed higher values of SNR and CNR, that make them more suitable for applications in the biomedical imaging. The negative controls for the PA tests in PE tubes consisted in a PWE tube loaded with phosphate buffered saline (PBS), and the Ex-vivo PA images processed for the data calculation were reported in Figures S2 and S3 (Supporting Information).

3.4. Photoacoustic Evaluation in Biological Environment on Ex-vivo Sample

To evaluate the PA potentialities of NPs in a realistic environment, three samples of chicken breasts were injected with 30 µL bolus of NPs, one of each to the concentration of 4 mg/mL. The physical properties of chicken breast samples simulate echogenicity similar to that observed in human tissues, leading to an effective realistic simulation. The second row of Figure 6 shows the PA spectral trends acquired in an injected slice of the samples (Figure $6b_1$), with the respective PHS (Figure $6b_2$), the typical PA spectral trend and PHS of a non-injected ex-vivo region was reported in Figure S3 (Supporting Information). Third row of Figure 6 shows the 3D PA-US volume reconstructions of NPs distributions inside the region of chicken breast samples injected with the NPs (Figure $6c_{1-3}$). The values of CNR and SNR were reported in **Table** 5. The PA effect stimulated inside the muscle tissue of the sample showed high values of CNR and SNR with a percentage of variation within 1 and 3.5. The PA imaging of the injected region (Figure $6c_{1-3}$) showed a strong and clear PA signal, useful as effectiveness contrast agent. As previously predicted from the photoacoustic characterization in phantom, the DHI-Ag_SiO_2 nanoparticles, when injected in a sample of biological tissue, simulating a real scenario, demonstrated their potential as photoacoustic contrast agent, showing high values of SNR and CNR, respectively 114 and 96 (Table 4). Comparing them with the obtained values of CNR and CNR from CAF and Gal-Ag_SiO_2 nanoparticles, the DHICA-Ag_SiO_2 nanoparticles resulted 200% more effective.

3.5. Hyperthermic Tests

To deeper explore these nano-architectures and their field of applications, we carried out test to check the thermal behavior under continuous wavelength (CW) laser illumination, throughout near infrared CW laser illumination at 808 nm. The CW laser stimulation led the NPs to get a temperature increase from room temperature (≈26 °C) up to 43 °C and over (Figure 6, b_3). In terms of temperature gradient, CAF-Ag_SiO_2, DHICA-Ag_SiO_2 and GAL-Ag_SiO_2 NPs showed respectively around 10, 15, and 16 °C. These important temperature gradients pave the way for a theranostic approach in their use. [43,44] Indeed, these kinds of nanoarchitectures already exhibit intrinsic antibacterial and antitumor effects properties, but also a thermal behavior, under CW laser illumination, capable to reach the right temperature range in a living being to be treated by hyperthermic therapy.

4. Conclusions

Hybrid melanin-based nanomaterials were synthesized using SiO2-templated approach from various synthetic or bio-available melanogenic precursors. In particular, XRD and TEM evidences proved that phenolic components act as reducing agents causing the formation of metallic Ag domains, whose distribution and size in the nanostructures are straightly related to the reduction kinetic of metallic component by melanogenic precursors. Thus, depending on the nature of organic starting compound, either metal core or surface exposed metal cluster site can result as a final architecture. The obtained hybrid NP has shown to increase antibacterial activity even at low concentrations and has a good photoacoustic signal. This is because of the highest reducing behavior of DHICA among the other organic moieties used, which leads to a core-shell architecture, exhibiting better PA performance. It is important to note that the PA effect stimulated inside the biological tissue of chicken breast samples showed high values of CNR and SNR, with a strong and clear PA signal. This makes it useful as an effective contrast agent. Finally, CAF-Ag_SiO_2, DHICA-Ag_SiO_2, and GAL-Ag_SiO_2 NPs showed relevant photothermal behavior, producing, respectively, ≈10, 15, and 16 °C temperature increase. These important results support multifunctional features and pave the way for numerous potential application prospects.

Supporting Information

Supporting Information is available from the Wiley Online Library or from the author.

Acknowledgements

The authors acknowledge MSC, PhD student Sebastiano Marra for the precious help in the artworks.

Conflict of Interest

The authors declare no conflict of interest.

Author Contributions

The manuscript was written through contributions of all authors. / All authors have given approval to the final version of the manuscript.

Data Availability Statement

The data that support the findings of this study are available on request from the corresponding author. The data are not publicly available due to privacy or ethical restrictions.

Keywords

Bio-available melanogenic precursors, hybrid silica-based particles, hyperthermic properties, photoacoustic imaging, theranostic nanoplatforms

Received: January 12, 2024
Revised: March 13, 2024
Published online: April 18, 2024

[1] S. Chen, Q. Zhang, Y. Hou, J. Zhang, X.-J. Liang, *Eur. J. Nanomed.* **2013**, *5*, 61.
[2] Y. Xiao, X. Hu, Q. Liu, Y. Zhang, G.-J. Zhang, S. Chen, *Inorg. Chem. Front.* **2023**, *10*, 4289.
[3] N. Van Hao, N. P. Hung, V. X. Hoa, N. T. Ha, N. T. K. Van, P. Van Trinh, *RSC Adv.* **2023**, *13*, 21838.
[4] A. Mavridi-Printezi, M. Guernelli, A. Menichetti, M. Montalti, *Nanomaterials* **2020**, *10*, 2276.
[5] H. Wang, C. A. Thorling, X. Liang, K. R. Bridle, J. E. Grice, Y. Zhu, D. H. G. Crawford, Z. P. Xu, X. Liu, M. S. Roberts, *J. Mater. Chem. B* **2015**, *3*, 939.
[6] J. Zeng, M. Cheng, Y. Wang, L. Wen, L. Chen, Z. Li, Y. Wu, M. Gao, Z. Chai, *Adv. Healthcare Mater.* **2016**, *5*, 772.
[7] X. Song, S. Yu, G. Jin, X. Wang, J. Chen, J. Li, G. Liu, H. Yang, *Small* **2016**, *12*, 1506.
[8] J. Qin, G. Liang, D. Cheng, Y. Liu, X. Cheng, P. Yang, N. Wu, Y. Zhao, J. Wei, *J. Colloid Interface Sci.* **2021**, *593*, 172.
[9] H. Liu, Y. Yang, Y. Liu, J. Pan, J. Wang, F. Man, W. Zhang, G. Liu, *Adv. Sci.* **2020**, *7*, 1903129.
[10] K. Tang, J. Xue, Y. Zhu, C. Wu, *Wiley Interdiscip. Rev. Nanomed. Nanobiotechnol.* **2023**, *16*, e1914.
[11] N. T. T. Nguyen, L. M. Nguyen, T. T. T. Nguyen, T. T. Nguyen, D. T. C. Nguyen, T. Van Tran, *Environ. Chem. Lett.* **2022**, *20*, 2531.
[12] Y. Ren, F.-Y. Wang, Z.-J. Chen, R.-T. Lan, R.-H. Huang, W.-Q. Fu, R. M. Gul, J. Wang, J.-Z. Xu, Z.-M. Li, *J. Mater. Chem. B* **2020**, *8*, 10428.
[13] H. Xu, Y. Zhang, H. Zhang, Y. Zhang, Q. Xu, J. Lu, S. Feng, X. Luo, S. Wang, Q. Zhao, *Coord. Chem. Rev.* **2023**, *488*, 215153.
[14] P. Yang, Z. Gu, F. Zhu, Y. Li, *CCS Chem.* **2020**, *2*, 128.
[15] L. Yang, X. K. Zhang, J. H. Zhang, J. F. Hu, T. Zhang, Z. P. Gu, Y. W. Li, *Acta Polym. Sin.* **2024**, *55*, 192.
[16] S. El Aanachi, L. Gali, S. N. Nacer, C. Bensouici, K. Dari, H. Aassila, *Biocatal Agric Biotechnol* **2020**, *29*, 101819.
[17] Y. Zou, X. Chen, P. Yang, G. Liang, Y. Yang, Z. Gu, Y. Li, *Sci. Adv.* **2020**, *6*, eabb4696.
[18] F. Amantea, G. Antignani, G. Pota, E. Cascone, S. Parisi, M. Alfè, V. Gargiulo, G. Luciani, A. Pezzella, G. D'Errico, *Appl. Surf. Sci.* **2023**, 157608.
[19] B. Silvestri, P. Armanetti, G. Sanità, G. Vitiello, A. Lamberti, G. Calì, A. Pezzella, G. Luciani, L. Menichetti, S. Luin, *Mater. Sci. Eng., C* **2019**, *102*, 788.

[20] G. Vitiello, A. Pezzella, A. Zanfardino, B. Silvestri, P. Giudicianni, A. Costantini, M. Varcamonti, F. Branda, G. Luciani, *Materials Science and Engineering C* **2017**, *75*, 454.
[21] D. L. Longo, R. Stefania, S. Aime, A. Oraevsky, *Int. J. Mol. Sci.* **2017**, *18*, 1719.
[22] I. Zmerli, J.-P. Michel, A. Makky, *Multifunctional Materials* **2021**, *4*, 022001.
[23] J. Park, H. Moon, S. Hong, *Biomater. Res.* **2019**, *23*. https://doi.org/10.1186/s40824-019-0175-9
[24] M. d'Ischia, K. Wakamatsu, A. Napolitano, S. Briganti, J. Garcia-Borron, D. Kovacs, P. Meredith, A. Pezzella, M. Picardo, T. Sarna, *Pigment Cell Melanoma Res* **2013**, *26*, 616.
[25] M. J. E. Fischer, *Surface plasmon resonance: methods and protocols* **2010**, 1.
[26] A. Blainski, G. C. Lopes, J. C. P. De Mello, *Molecules* **2013**, *18*, 6852.
[27] G. Pota, A. Zanfardino, M. Di Napoli, D. Cavasso, M. Varcamonti, G. D'Errico, A. Pezzella, G. Luciani, G. Vitiello, *Colloids Surf. B Biointerfaces* **2021**, *202*, 111671.
[28] N. Badalamenti, A. Modica, V. Ilardi, M. Bruno, V. Maresca, A. Zanfardino, M. Di Napoli, G. Castagliuolo, M. Varcamonti, A. Basile, *Nat. Prod. Res.* **2022**, *36*, 5842.
[29] P. Russo, A. Costantini, G. Luciani, F. Tescione, M. Lavorgna, F. Branda, B. Silvestri, *J. Appl. Polym. Sci.* **2018**, *135*, 46006.
[30] X. Zhang, H. Sun, S. Tan, J. Gao, Y. Fu, Z. Liu, *Inorg. Chem. Commun.* **2019**, *100*, 44.
[31] C. Thummaneni, D. V. S. Prakash, R. Golli, M. Vangalapati, *Mater Today Proc* **2022**, *62*, 4001.
[32] M. Ahani, M. Khatibzadeh, *Inorganic and Nano-Metal Chemistry* **2022**, *52*, 234.
[33] B. Bartolomei, G. Gentile, C. Rosso, G. Filippini, M. Prato, *Chemistry* **2021**, *27*, 16062.
[34] Z. Ji, X. Shen, X. Yue, H. Zhou, J. Yang, Y. Wang, L. Ma, K. Chen, *J. Colloid Interface Sci.* **2015**, *459*, 79.
[35] Y.-S. Liu, Y.-C. Chang, H.-H. Chen, *J. Food Drug Anal.* **2018**, *26*, 649.
[36] J. Chen, J. Yang, L. Ma, J. Li, N. Shahzad, C. K. Kim, *Sci. Rep.* **2020**, *10*, 2611.
[37] D. Guo, D. Dou, L. Ge, Z. Huang, L. Wang, N. Gu, *Colloids Surf. B Biointerfaces* **2015**, *134*, 229.
[38] J. Zhao, A. O. Pinchuk, J. M. McMahon, S. Li, L. K. Ausman, A. L. Atkinson, G. C. Schatz, *Acc. Chem. Res.* **2008**, *41*, 1710.
[39] K. Nemčeková, V. Svitková, J. Sochr, P. Gemeiner, J. Labuda, *Anal. Bioanal. Chem.* **2022**, *414*, 5493.
[40] S. L. Smitha, K. M. Nissamudeen, D. Philip, K. G. Gopchandran, *Spectrochim. Acta. A Mol. Biomol. Spectrosc.* **2008**, *71*, 186.
[41] V. Venezia, G. Pota, B. Silvestri, G. Vitiello, P. Di Donato, G. Landi, V. Mollo, M. Verrillo, S. Cangemi, A. Piccolo, *Chemosphere* **2022**, *287*, 131985.
[42] G. Pota, G. Vitiello, V. Venezia, F. D. Sala, A. Borzacchiello, A. Costantini, L. Paduano, L. P. Cavalcanti, F. Tescione, B. Silvestri, G. Luciani, *Polymers (Basel)* **2022**, *14*, 3568.
[43] Y. Liu, F. Li, Z. Guo, Y. Xiao, Y. Zhang, X. Sun, T. Zhe, Y. Cao, L. Wang, Q. Lu, *Chem. Eng. J.* **2020**, *382*, 122990.
[44] V. O. Shipunova, M. M. Belova, P. A. Kotelnikova, O. N. Shilova, A. B. Mirkasymov, N. V. Danilova, E. N. Komedchikova, R. Popovtzer, S. M. Deyev, M. P. Nikitin, *Pharmaceutics* **2022**, *14*, 1013.